

Cost effective measuring technique to simultaneously quantify 2D velocity fields and depth-averaged solute concentrations in shallow water flows



Santiago Rojas Arques*, Matteo Rubinato, Andrew Nichols, James D. Shucksmith

Department of Civil and Structural Engineering, The University of Sheffield, Mappin Building, S1 3JD Sheffield, UK

ARTICLE INFO

Keywords:

Flume experiment
Particle Image Velocimetry (PIV)
Planar Concentration Analysis (PCA)
Cost-effective
GoPro Hero4

ABSTRACT

This paper presents a cost-effective methodology to simultaneously measure mixing processes and surface velocity fields in shallow flows using multiple, synchronized low cost cameras and lighting. Velocity fields and depth averaged concentration of a soluble fluorescent tracer are obtained over a $4.8 \times 1.22 \text{ m}^2$ measurement area using the new techniques and the results verified against traditional point probe measurements in a laboratory flume. An example of simultaneous velocity/concentration measurement is presented for an instantaneous release of tracer into flow around an obstruction. The method will help to improve the understanding of mixing processes in shallow open channel flows. It is anticipated that the technique will be useful in physical modelling studies where the mixing and hydraulic length scales under investigation are in the order of 1–10 m, for example in compound channels and partially vegetated streams.

1. Introduction

Understanding the mechanisms behind the transport and mixing of soluble pollutants is necessary to enable the effective management of surface water bodies such as rivers and lakes. Experimental studies of solute transport are commonly used to understand and quantify mixing processes in hydraulically complex open channel flows such as compound channels [52], sinuous channels [34,9] and vegetated flows [37,38,42]. Mixing processes are driven by turbulent diffusion processes at small scales as well as larger scale flow structures driven by differential advection and secondary currents (i.e. dispersion). It is therefore often desirable to obtain simultaneous measurements of concentration and velocity/turbulence fields, such that these processes can be related over the key length scales of interest.

The most commonly used methods to quantify solute transport processes involve the injection of a dye or saline tracer into the flow. The resulting downstream concentration field is traditionally measured via point measurements taken with fluorimeters (for dye tracers) [28,36], conductance meters (for saline tracers), fluorescent dye radioisotope tracers [35] or synthetic gas [15] but these approaches can be time-consuming and laborious depending on the number of measurement points and the duration of each measurement. In particular, measurement of concentration fields that are both temporally and spatially variable in the near to mid field zones (before full cross

sectional mixing is achieved) is practically difficult. Such techniques also generally preclude the simultaneous measurement of velocity/turbulence due to instrument obstruction. Whilst other cost-effective techniques using thermographic cameras have been applied in order to study turbulence phenomena and mixing processes in rivers, e.g. [12,3], these methodologies are limited by the need to maintain a minimum temperature difference of around 50 Celsius between the ‘tracer’ and the bulk flow discharge, which may generate additional flow complexities due to convection effects.

More sophisticated quantitative measurements of dye concentration by light attenuation techniques have been conducted in shallow turbulent free-surface flows. Ward [47] reported an early study measuring concentrations of dye in laboratory channels, while Barbatusi et al. [4] and Balachandar et al. [5] obtained pointwise dye concentrations using an intrusive light absorption probe. Balachandar et al. [6] and Balu et al. [7] reported instantaneous dye concentration measurements using a video imaging technique in the shallow wake generated by a flat plate. Rummel et al. [31] investigated experimentally a depth-averaged analysis of mass concentration in shallow turbulent flows providing a new time/cost efficient and easy-to-use measuring technique called Planar Concentration Analysis (PCA) which allows to evaluate the depth-averaged concentration of a soluble conservative tracer. A single camera was used recording an area of $1.4 \times 1 \text{ m}^2$ and, in order to obtain a bigger observation area, the

* Corresponding author.

E-mail addresses: srojasarques1@sheffield.ac.uk (S. Rojas Arques), m.rubinato@sheffield.ac.uk (M. Rubinato), a.nichols@sheffield.ac.uk (A. Nichols), j.shucksmith@sheffield.ac.uk (J.D. Shucksmith).

<https://doi.org/10.1016/j.flowmeasinst.2018.10.022>

Received 6 February 2018; Received in revised form 17 May 2018; Accepted 21 October 2018

Available online 23 October 2018

0955-5986/© 2018 The Authors. Published by Elsevier Ltd. This is an open access article under the CC BY license (<http://creativecommons.org/licenses/by/4.0/>).

experiment was repeated in three different positions at different times. Zhang et al. [51] and Chu et al. [14] used a video imaging technique to study the mass spreading of a shallow jet released in a stagnant water body. Video image information from observed dye solutions were converted to quantitative mass concentrations by performing a calibration procedure spatially averaged over the area of observation. Both Balachandar et al. [6] and Zhang et al. [51] fitted an empirical transformation function to spatially averaged brightness values of known concentrations, while Balu et al. [7] applied a neural network approach to convert red/green/blue (RGB) values to dye concentrations. Carmer et al. [13] constructed a PCA system to observe the large-scale eddy structures and mixing of a tracer mass in a shallow turbulent free-surface flow around a large cylindrical obstacle. Similar to Rummel et al. [31], a single camera in three different positions was used, recording an area of $1.6 \times 1.2 \text{ m}^2$ each time. However these studies required sophisticated lighting setups involving lasers or light diffusers.

To obtain velocity-field datasets, Particle Image Velocimetry (PIV) techniques are commonly used. PIV is a technique which uses pairs of camera images capturing a planar array of points to determine the vector displacement of these points between the two images at defined locations (interrogation areas). With Surface Particle Image Velocimetry (SPIV), the points take the form of buoyant particles scattered on the surface of a water flow [48,26,27]. The images are divided into interrogation areas, and a 2D cross-correlation is applied to each interrogation area to determine the displacement which, coupled with the time step between images, yields the local velocity vector. Surface PIV is easier to implement than traditional PIV, as the particles do not have to be neutrally buoyant, the field of view can be much larger, and no complex laser and camera arrangements are generally required. However, it only provides surface velocity data, so is generally only applicable for shallow flows. The initial groundwork for PIV theory was laid down by [1] who described the expected value of the auto-correlation function for a double-exposure continuous PIV image. This description provided the framework for experimental design rules [19]. Electronic cameras enable the direct and rapid recording of the particle images [50,48,11]. Applications of PIV range from slowly creeping flows such as those examined by [33], who measure both instantaneous and mean velocity flow in micro-scale fluid devices using a micro-scale PIV; to detonations lasting only a few tens of microseconds such as those examined in [25], who applied the PIV technique to study moving millimeter shock waves, from nanoscale flow phenomena [43], who used a novel non-intrusive technique to obtain the shape of walls studying flow around them with a precision of nanometers, to motion in the atmosphere of Jupiter [44]. Moreover, PIV application range goes from the motion in the beating heart of vertebrate embryos [16,46], where velocity distribution of blood were studied to obtain shear stress distributions to the accidental release of oil at the bottom of the Gulf of Mexico [23,22] where flow rate of the oil escaping from the well to the sea was studied. What all of these studies show is that PIV is an incredibly versatile and data-rich technique, but they all use equipment that is relatively expensive (such as lasers, microscopes, cameras) for optimal results, prohibiting the widespread implementation of PIV, particularly in challenging environments. PIV has been reviewed in the literature several times [1,45,49,18] and is also the subject of at least two books [29,2]. The most recent book presents the current state of the art for PIV in its broad sense, i.e., including approaches such as particle tracking velocimetry (PTV), microscopic PIV, tomographic PIV, and holographic PIV. PIV and PCA have begun to be combined [13], but so far only for small scale laboratory flows and not simultaneously due to the cost and complexity of the equipment used. To the authors' knowledge, to date, no previous studies have combined PIV and PCA measurement synchronously. This study aims to present the opportunity for future large-scale laboratory and field measurement of simultaneous 2D velocity and depth averaged scalar fields of solute concentration. The technique utilises a low-cost and wide field of view measurement system consisting of multiple, linked GoPro Hero4

cameras instead of one single camera, increasing the observation area and decreasing experimental time. Furthermore, this new technique can be implemented without any sophisticated lighting setups or light diffusers. Sections 2.4.1 and 2.5.1 provide a verification of new large scale surface PIV and PCA techniques vs established measurement methodologies (ADV probes and 'Cyclops' point fluorescence probes) for data gathered in an open channel flow flume, and Section 3 provides an example of synchronously combined PIV and PCA measurement for a temporally and spatially variable dye release in an open channel flow featuring obstructions.

2. Methodology

2.1. Experimental setup

Testing was undertaken within the University of Sheffield hydraulics laboratory. The experiments described were conducted in the main flume which was constructed of reinforced glass fibre panels. The bed was composed of panels of 1.5 mm thick perforated stainless steel, with 6 mm diameter holes in a hexagonal arrangement with 9 mm pitch, providing a uniform bed roughness. The flume has an experimental length of 14.5 m, a width of 1.22 m and depth of 0.5 m and was set at a fixed slope of 0.00123. The slope of the channel was confirmed by measuring the depth of a stationary body of water along the length of the channel. Upstream of the experimental section the flume is fitted with a flow baffle. Downstream of the experimental section the flume is fitted with a tailgate weir so that uniform flow can be achieved. Discharge through the channel can be controlled by use of a valve regulating flow from the main laboratory constant-head tank (Fig. 1). The constant head tank is fed from the main laboratory sump via a pump. Four uniform flow conditions were examined, ranging in depth from $D = 36$ to 90 mm , with mean velocity from $U = 0.23$ to 0.4 m/s . The flow conditions are described in Table 1, and are representative of typical 'gentle gradient streams' [30]. The examples used to describe the measurement and analysis procedure are related to one flow condition ($D = 90 \text{ mm}$), but are representative of the procedure used for all flow conditions examined.

2.2. Instrumentation and equipment

2.2.1. Cameras

Four GoPro Hero 4 Black Edition cameras have been used to acquire video images during the experiments to be used for the application of the Particle Image Velocimetry (PIV) and Planar Concentration Analysis (PCA) techniques. The cameras were set to record video frames of size 1440×1920 pixels. The maximum frame rate for this resolution, 80 Hz , was selected in order to minimise exposure time and hence reduce motion blur on the particles. The cameras were positioned at a height of 1.2 m above the flume bed, giving a resolution of approximately 1 mm per pixel at the centre of the images. This also ensured that each PIV seeding particle was represented by a cluster of at least 5 pixels, giving good particle definition and ensuring accurate detection by the PIV software. Each camera captured a field of view which included the full width of the flume, and a streamwise distance of approximately 2.5 m. However, due to lens distortion, the upstream and downstream edges of the frames were strongly distorted, and were hence cropped so that the streamwise length of the frames was 1.4 m. The cameras were positioned above the centreline of the flume, distributed in the streamwise direction at intervals of 1.2 m. This enabled a 200 mm overlap between adjacent cameras, and an overall field of view of 5 m in length.

2.2.2. Particle dispenser

Successful surface PIV measurements are dependant on physical properties of the particles and the distribution of them on the water surface. They must give a contrast against the flume bed, the density

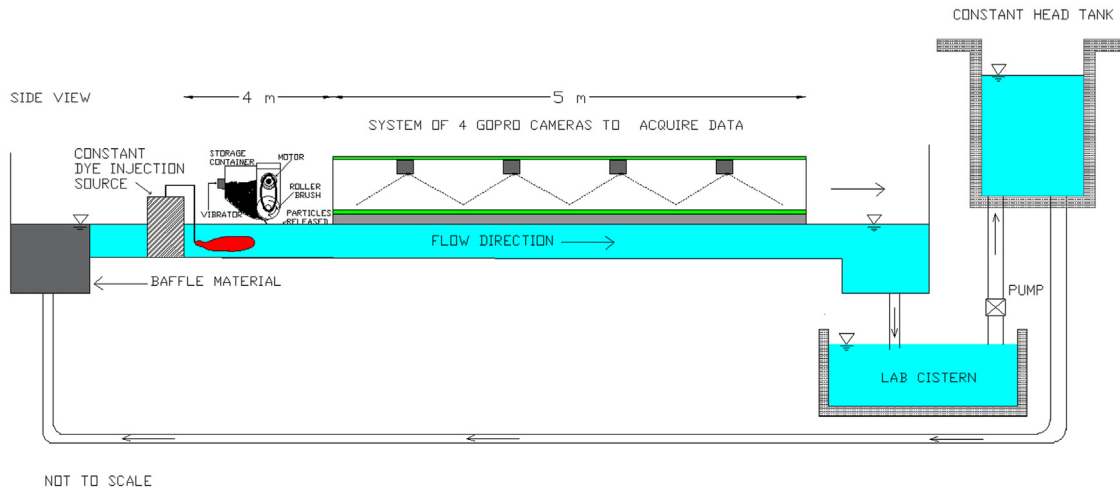


Fig. 1. Longitudinal profile of the experimental model.

Table 1
Flow conditions examined.

Test ID	Water Depth (D) [mm]	Flow rate (Q) [l/s]	Flow velocity (U) [ms ⁻¹]	Re [-]	Shear velocity (u*) [ms ⁻¹]
Run I	36	10.2	0.23	8400	0.020
Run II	54	19.4	0.29	15,900	0.024
Run III	72	33.1	0.38	27,200	0.028
Run IV	90	43.6	0.40	35,700	0.031

must be lower than that of water, and the size must be sufficient to allow individual particles to be discerned from the camera image. It was found that sufficient visualization can be obtained using the cameras employed here (described in 2.2.1) with 2 mm black polypropylene particles [48]. Also, the particles should be distributed uniformly in the lateral and longitudinal directions, with sufficient density to allow several particles to be present in each PIV interrogation area. For this purpose, a particle dispenser was designed to uniformly release the buoyant particles onto the surface of the flow in the flume. This comprises a hopper, a roller brush and an eccentric rotary vibrator. The velocity of the brush can be continuously varied between 0 and 20 rpm to control the particle release rate. The brush ensures an equal particle distribution over the whole flume width. The tracer particles are stored in a hopper behind the brush, while the vibrator is installed on the container to mobilise the particles and ensure a constant and uniform particle supply to the brush. The vibrator shakes the metal wall of the storage container at around 25 Hz. The hopper was designed to accommodate enough particles to supply the maximum possible requirements as follows:

- high, 1 m/s, flow velocity;
- small, 2.5 cm, PIV interrogation areas;
- at least 6 particles per interrogation area;
- 3 mm particles (in reality they are 2–3 mm);
- very loose packing (60% volume fraction) – in truth the vibrator helps to pack them closer;
- 10 min measurement time.

The resulting distribution of the particles is approximately uniform, containing at least 5–6 particles within the area of the interrogation windows used in the PIV analysis (see Section 2.4). This density of seeding is considered suitable for the application of PIV measurement [48].

2.2.3. Dye injection

The injection system consisted of a constant head tank feeding Rhodamine WT dye to a vertical pipe (4 mm diameter), with 1 mm holes drilled at intervals of 10 mm. By covering the holes above the water line, the holes within the water would release several continuous streams of dye into the flow in order to promote uniformly well mixed conditions in the vertical direction. To ensure vertically well mixed conditions the injection position was 4 m upstream of the measurement section (over 40 water depths).

2.3. Image techniques

2.3.1. Spatial calibration

For each video recording, the frames were dewarped to correct for lens distortion and rotation of the camera relative to the flume, and cropped to eliminate pixels outside the area of interest. The dewarping and cropping was achieved via a spatial calibration. A chequerboard pattern was placed on the flume bed beneath each camera in turn (Fig. 2a). The elevation of the grid was set to coincide with each of the planned flow depths given in Table 1, and images were recorded. A standard Matlab algorithm, called “FITGEOTRANS”, then identified the vertices of the chequerboard, and used these to determine a piecewise linear transformation which would map the camera images onto an orthogonal Cartesian coordinate system. The Matlab algorithm uses a 2D Piecewise Linear Transformation using pairs of points, “Moving Points” and “Fixed Points”. This algorithm divides the plane into local regions where different functions are applied to convert “Moving Points” into “Fixed Points” obtaining an orthogonal Cartesian coordinate system [21]. A spatial calibration was thereby calculated for each flow depth for each camera. Fig. 2a shows examples of (left) an original image, (central) the result of the dewarping procedure, and (right) the dewarped and cropped image area. The resolution of the output images was selected to maintain the maximum spatial resolution from the original images, whereby 1 pixel in the camera plane corresponds to 1 mm on the calibration plane. The calibration procedure was performed for all 4 cameras, and at each of the flow depths examined in this work. This meant that the flow images during the experimental tests could be dewarped and cropped according to these spatial calibrations. When reproducing the points in the calibration chequerboard, the reproduction error of the camera images was found to have a mean value of 0.08 mm for camera 1, 0.09 mm for camera 2, 0.09 mm for camera 3 and 0.09 mm for camera 4.

2.3.2. Synchronization

In order for the combined images from all 4 cameras to provide

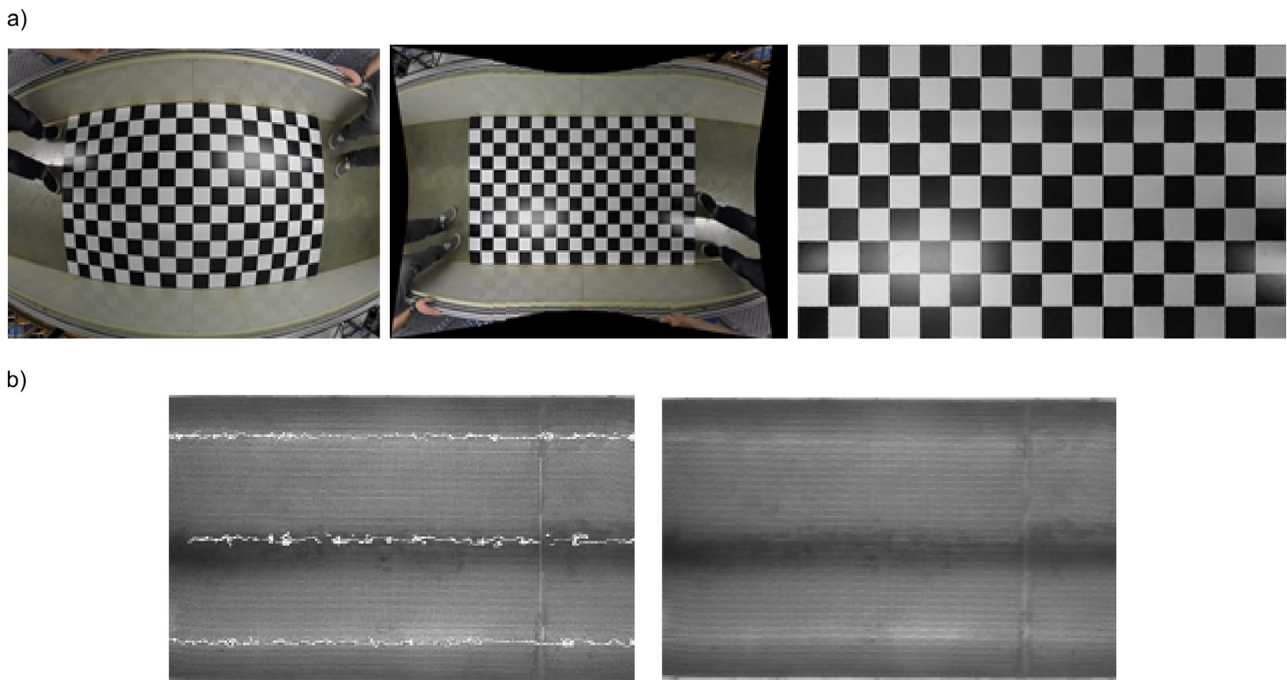


Fig. 2. a) Chequerboard pattern placed on the flume bed beneath each camera and de-warping procedure displayed and b) PCA data with direct LED reflections eliminated and decimated to 10×10 mm image resolution.

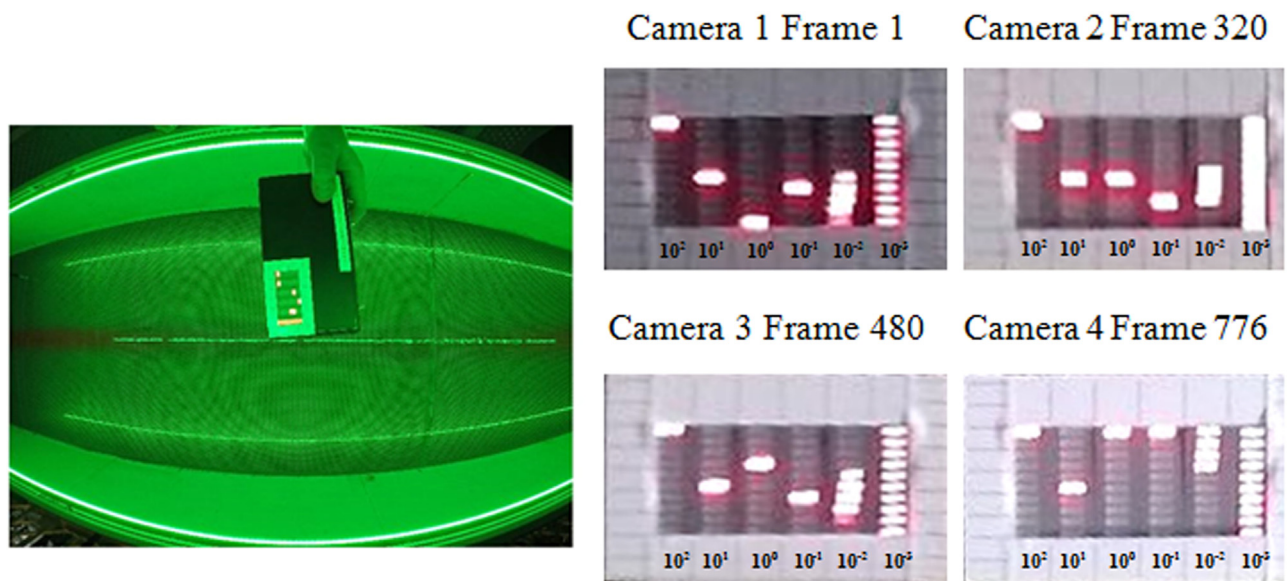


Fig. 3. Left image shows a frame recording the LED timer used during experiments. Right images show frames of the LED timer recorded for each camera and their corresponding frame.

unambiguous data, it was necessary that the cameras record images synchronously. This would also enable reconstruction of instantaneous velocity fields and/or concentration maps. As a first approximation, this was achieved via the GoPro WiFi Remote control, however the remote trigger could only synchronise the cameras to within 0.1 s, or 8 frames. In order to reduce the error, camera recordings would need to be synchronised to at least the nearest frame. This was achieved by the construction of an LED timer to provide an external absolute time reference to each camera. Fig. 3 shows the LED timer used which consisted of a bank of 6 columns of 10 LEDs. Analogue circuitry controlled the LED output so that the right-most column illuminated one by one at a rate of 1 ms, before returning to zero. Each subsequent column was set to switch at a rate ten times slower than the column to its right, such that

the left-most column updated at a rate of 100 s. In this manner an absolute time between 0 and 1000 s can be read from the device, to the nearest ms. Once the cameras were all triggered by the WiFi remote, the LED timer was introduced below each camera in turn. This allowed an absolute time reference to be extracted for at least one frame of each camera recording. Given the camera sample rate this time frame was extrapolated for the rest of the frames in all recordings. This enabled the camera recordings to be synchronised to the nearest frame. In the event that the frame offset is not an integer number, the LED timer data could be used to interpolate the final values of flow velocity field or concentration map, though this level of accuracy was not required in the present study.

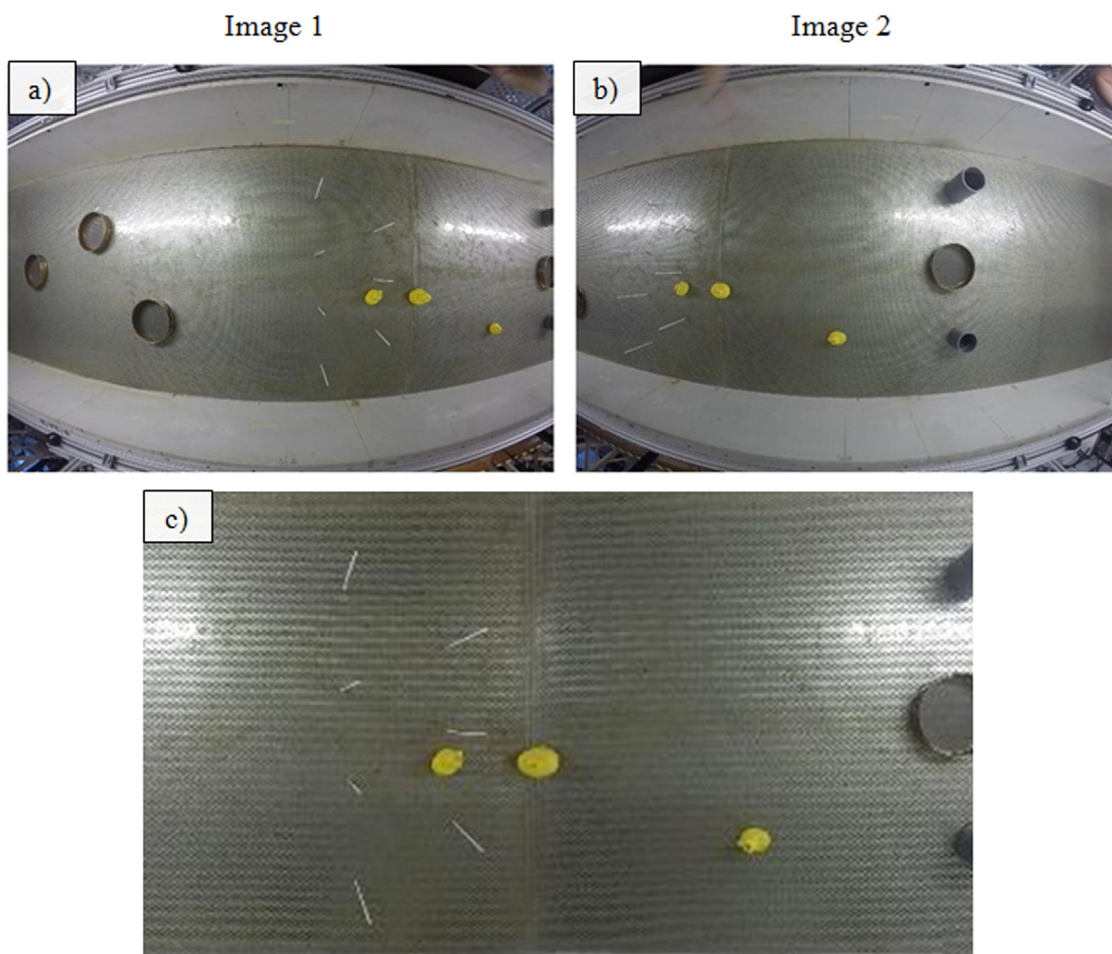


Fig. 4. Two stitched images before stitching (4a and 4b) and the final combined image (4c) after spatial calibration, synchronisation and image stitching/smoothing are applied.

2.3.3. Stitching

With the cameras calibrated, the overlapping field of view meant that the synchronised images from all the cameras could be combined to produce images and videos over a very large spatial domain (5×1.2 m). During the spatial calibration of each camera, the exact relative location of the calibration grid in each case was noted. This meant that the overlap in the field of view of two adjacent cameras was known to the nearest millimeter, and adjacent camera images were thereby combined as shown in Fig. 4. In order to avoid a discontinuity in the combined images, a smoothing function was applied to generate a gradual transition from one camera image to the next over the overlap region. This function was composed of a weighted average of the RGB values of each camera, whereby the weighting of one camera decreased sinusoidally from unity to zero, while the weighting on the next camera increases sinusoidally from zero to unity. Fig. 4 shows an example of two stitched images before (Fig. 4a and Fig. 4b) and after (Fig. 4c) the stitching and smoothing functions are applied. Additionally, Fig. 4 illustrates the transit of a large floating tracer across the transition from one camera to the next, demonstrating that the synchronisation and stitching process functions appropriately (Fig. 4c).

2.3.4. PCA illumination

Since the Rhodamine WT dye absorbs green (500–575 nm) light [40,24], three arrays of 550 nm LEDs were installed along the flume, two along the upper edges of each sidewall, and one suspended above the centreline. This provided a near-uniform green illumination to the measurement area. As the Rhodamine WT concentration was increased, the measured intensity of the green component of the cameras would be

reduced, as more green light was absorbed.

In some regions the mean intensity was corrupted by the direct reflection of the green LED lighting in the water surface, but the slight fluctuations present in the water surface meant that the position of these direct reflections varied with time across the image plane. To produce a time-resolved image, the directly reflected component could therefore be removed by taking the median value of each pixel over time. This is illustrated in Fig. 2b which shows an instantaneous image (green component), and an image composed of the median value of each pixel over a short measurement time (20 s). The resulting intensity maps were of size 1400×1220 . To perform a dye concentration calibration, and subsequently apply that calibration, for each individual pixel location would be incredibly computationally demanding. For this reason the number of rows and columns were each decimated by calculating the average of 10×10 cells of pixels. This resulted in intensity maps of size 140×122 points (10 mm resolution). This process also helped to remove any remaining erroneous colour points, and reduced the size of the images while still maintaining a good spatial resolution for PCA measurements of 10 mm in each direction.

2.4. PIV data analysis

In order to prepare the images for analysis, the mean (background) image was calculated over the measurement time. The instantaneous images were then subtracted from this background image, such that the background would turn black, while the particles would remain bright. This was designed to remove the pattern of the perforated stainless steel base, which would otherwise generate ambiguity and bias toward

multiples of 9 mm (the bed perforation pitch) in the PIV displacement analysis. This process was performed for each frame of each camera recording during 20 s, and the synchronous images from the 4 cameras were then combined to produce a single wide image of the particles in the entire measurement section. These images were then supplied to the commercial PIV software Dynamic Studio, by *DantecDynamicsLtd*. An adaptive correlation was performed to determine the velocity field for each adjacent image pair. A range validation was applied to remove spurious high velocities, and zero velocities resulting from interrogation areas with no seeding particles. For each flow condition the filter removed less than 5% of the velocity vectors. The rejected vectors were then replaced via a 5×5 moving average routine. The velocity matrix vectors were then exported for analysis in Matlab®. Mean velocity value at each transverse point and the corresponding standard deviation was calculating, obtaining a PIV range.

2.4.1. PIV validation

Two methods were used to validate the PIV velocity data. Firstly a manual measurement of velocity was made by timing the transit of a small patch of floating particles over a streamwise distance of 6 m. This was done for three spanwise positions, 150 mm, 250 mm and 600 mm from the flume sidewall. The measurements were repeated three times each by two different individuals in order to quantify the error in the measurements. The second method applied to validate the PIV data utilised measurements collected by using an Acoustic Doppler Velocimetry (ADV) probe situated in the middle of the PIV measurement area. Three spanwise positions were selected, 150 mm, 300 mm and 600 mm from the flume sidewall. In each spanwise position, between 6 and 13 different vertical locations were measured (depending on the water depth considered), from adjacent to the bed to very near the water surface. Instantaneous velocity values were measured in the three main directions (x, y and z) for a duration of 60 s with a sampling rate of 160 Hz. The signals collected were filtered with an ADV despiking technique [17,8]. To compare with surface velocities measured with the PIV techniques, a logarithmic function was fitted through the profile of streamwise velocities measured over the flow depth for each flow condition. In each case the logarithmic profile gave a good fit to the observed data (mean $R^2 = 0.95$) with a fixed equivalent roughness height of 0.3 mm. Appropriate surface flow velocities for comparison were extrapolated from each profile.

Fig. 5 shows the automated PIV output for the four flow conditions listed in Table 1 (plotted as range between minimum and maximum velocity values over the measurement length), along with i) black markers to show the validation data captured manually and ii) red markers representing the surface flow velocity derived from the ADV measurements. It can be noted from Fig. 5 that the overall velocity values obtained with the PIV technique are within the range of velocities recorded manually and measured with the ADV. Some variances (mean difference $\pm 5.17\%$ between PIV and manual measurements, $\pm 4.26\%$ between PIV and ADV) may be due to the effects of light reflections that are not completely removed from the raw images, affecting the instantaneous images assembled for the PIV software. Despite this, the results confirm that the PIV technique applied is suitable to estimate the surface velocity fields.

2.5. PCA calibration and data analysis

In order to relate the concentration to the light intensity recorded at each of the 140×122 measurement points, a calibration was performed. A 6.4 m long section of the flume, which contained the measurement section, was hydraulically isolated using two sealed blockages. Concentration solutions were then fully mixed in the isolated flume section for a range of flow depths.

Ten different concentrations were recorded in order to characterize the intensity response to the dye concentration at each measurement point. The concentrations used are given in Table 2. This was conducted for four water depths ranging from 36 mm to 90 mm in 18 mm increments (i.e. the same depths used for the flow tests and the spatial calibration). For each measurement, video was recorded on each camera for a period of 10 s. The calibration images were then digitized and pre-processed in the same way as the video images of the actual flow observations, via the spatial calibration procedure described in Section 2.3.1.

To obtain intensity values 10 s of recording data was taken. For each 10 by 10 pixel area in the measurement plane, and for each of the water depths examined, the median intensity of the green component was examined for each of the ten concentrations used (as discussed in Section 2.3.4). Fig. 6 shows an example of the relationship between concentration and green intensity for a single 10 by 10 measurement area. In this figure the relationship for each depth was plotted for the

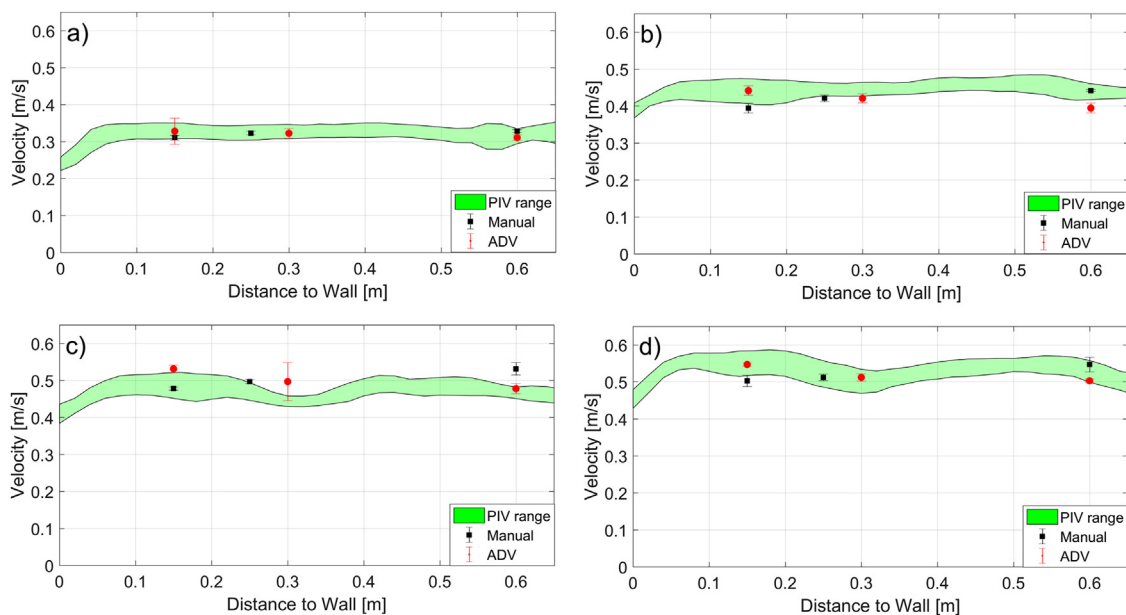


Fig. 5. Comparison of longitudinal velocity distributions between PIV results (range over measurement length), manual and ADV measurements (Run I = case a, Run II = case b, Run III = case c and Run IV = case d).

Table 2
Concentration values used for the calibration.

Test Number	1	2	3	4	5
Concentration (mg/l)	0	1.07E-06	2.13E-06	3.19E-06	4.25E-06
Test Number	6	7	8	9	10
Concentration (mg/l)	5.31E-06	6.36E-06	7.42E-06	8.47E-06	9.51E-06

same camera and measurement point. The relationship shows a decreasing intensity with an increasing concentration. This result agrees with the calibrations obtained by Rummel et al. [31] and Carmer et al. [13]. In order to fit an expression to this relationship, it was found that the intensity was best related to the concentration by a third order polynomial, as shown in Fig. 6, with observed intensity becoming insensitive to increasing concentration above approximately 0.65×10^{-5} mg/l (although some variation with flow depth is observed). Coefficients representing the best fit polynomial regression were calculated for each measurement area within the image frame. This would theoretically allow any recorded green intensity to be converted to a depth-averaged concentration value at each measurement point. For each measurement point, the maximum error (difference between the calibration data and the fitted expression) was also determined.

2.5.1. PCA validation

In order to validate the PCA technique, the concentration field downstream of a continuous injection of a soluble tracer are quantified and compared using the PCA technique and conventional point probes (Cyclops-7F™ submersible sensors). Due to instrument obstruction and different instrument sensitivity levels it was not possible to directly compare PCA and Cyclops measurements directly over the same test. Instead measured properties of the concentration field downstream of a continuous injection are compared in terms of extent, variance and ADE transverse mixing coefficients (Run IV).

2.5.2. Cyclops data analysis

Cyclops measurements were taken using Cyclops-7F™ submersible sensors. Four transverse profiles at 5, 6, 7 and 8 m downstream of the injection point were obtained (within the field of view of the camera system). At each profile 20 points were measured; at least 16 were taken at 20 mm resolution within the dye plume with the remaining points used to establish background concentration values. To ensure reliable values were obtained each measurement was collected over

20 s and temporally averaged. Background levels were removed from each profile, and the values lower than 3 % of the peak were also removed to eliminate the effect of instrument noise. Post filtering, the mass of each measured profile was observed to be within 2.2%, indicating good levels of mass conservation. A mass balance correction factor was nonetheless applied to profiles measured 6, 7 and 8 m downstream of the injection point.

2.5.3. PCA data analysis

PCA data was obtained for the 4 different depths ($D = 36, 54, 72$ and 90 mm) downstream of the continuous injection point. The concentration data had a resolution of 10×10 mm over the measurement area.

Prior to dye injection background levels for each measurement point were obtained from 20 s of recorded data. Once the injection was established, measurements were taken over 20 s, and the measured background levels were removed from each measurement point.

Individual profiles which suffered from a high level of noise were removed, and a 6th-order one dimensional median filter was applied to each remaining profile to eliminate noise. All values smaller than 3% of the maximum concentration of each profile were removed in order to eliminate the effect of instrument noise and to identify the start and end of each trace. Post filtering, the mass of each measured profile was observed to be within 5 %, indicating good levels of mass conservation. This is similar to levels observed in previous studies of mixing processes using traditional measurement techniques i.e. [10,39]. A mass balance correction factor was applied to profiles measured downstream of the injection point.

Fig. 7 compares the shape of the resulting non-dimensional concentration profiles from PCA and Cyclops measurements 5, 6, 7 and 8 m downstream from the injection point respectively. The PCA error range has been estimated based on variations observed in the calibration process between measured concentrations and the fitted calibration functions. Overall a good match is observed between concentration profiles quantified using PCA and Cyclops measurements. There is a small but consistent variation at the centre of each profile ($y = 0.6$ m) where PCA values are lower. This is likely to be caused by the effects of direct light reflections in the water surface affecting this measurement region that are not completely removed by the median filter technique previously described. These reflections may also slightly affect the concentration values on the left of each profile ($y = 0.3$ m), where concentration values obtained using PCA are also observed to be smaller than with the Cyclops. This indicates that some further refinements to account for these effects in the areas affected by direct light reflections would further improve the technique applied.

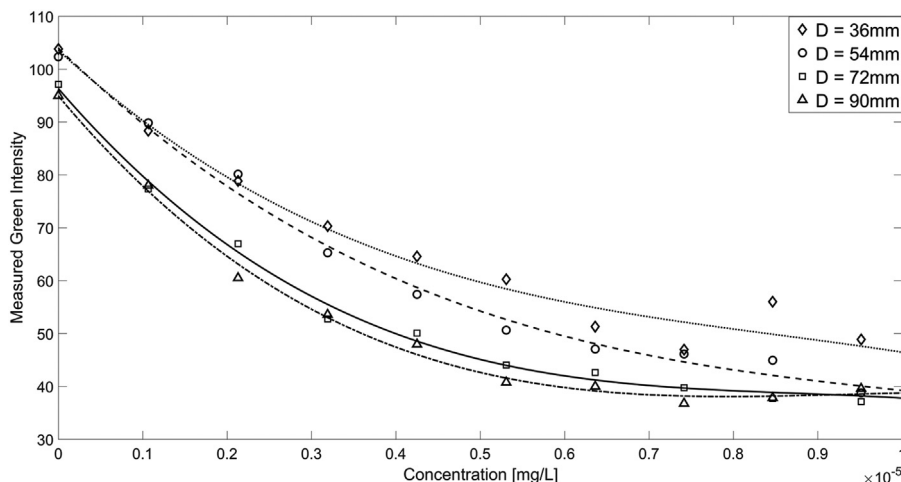


Fig. 6. Example of concentration vs mean green intensity in the image frame for a specific 10×10 pixel area for one camera and different water depths fitted using a 3rd order polynomial function.

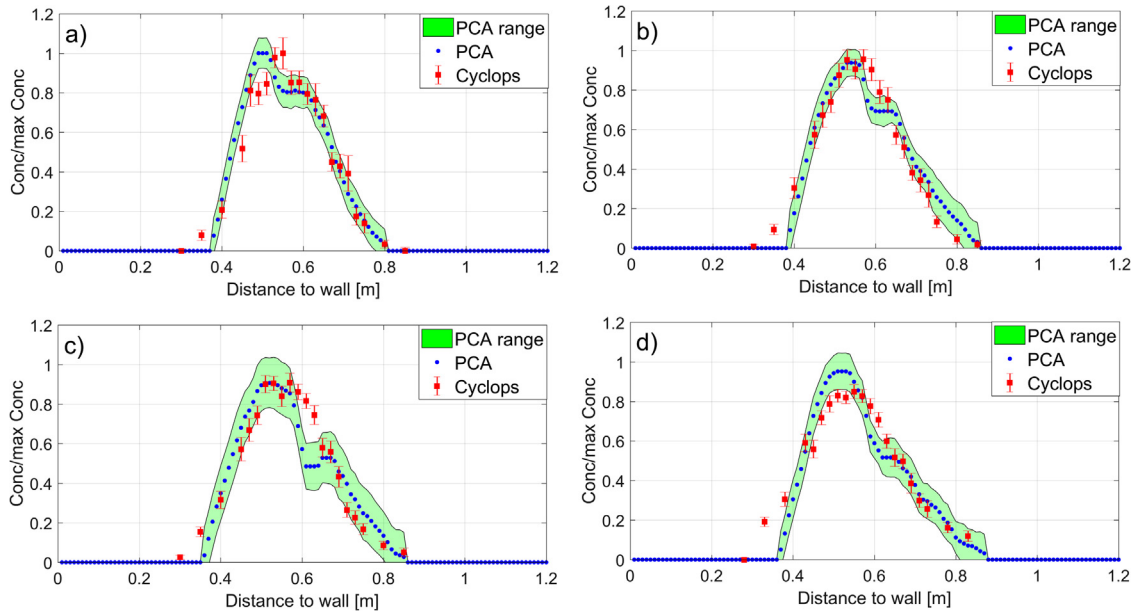


Fig. 7. Comparison between PCA and Cyclops non-dimensional transverse concentration profiles (Run IV, case $a = 5\text{ m}$, case $b = 6\text{ m}$, case $c = 7\text{ m}$ and case $d = 8\text{ m}$ from injection point).

Pearson's correlation coefficients were calculated using Eq. (1) for the each profile.

$$r = \frac{N \sum xy - (\sum x \sum y)}{\sqrt{[N \sum x^2 - (\sum x)^2][N \sum y^2 - (\sum y)^2]}} \quad (1)$$

Where N is the sample size, x and y are PCA and Cyclops datasets. The correspondent correlation factors calculated between PCA and Cyclops results displayed in Fig. 7 are $r_{5m} = 0.97$ and $r_{6m} = 0.98$ $r_{7m} = 0.95$ and $r_{8m} = 0.93$ for profiles at 5, 6, 7 and 8 m respectively.

To further verify PCA measurements a comparison between development of the spatial variance of the concentration profiles downstream of the injection position is presented in Fig. 8 for the $D = 90\text{ mm}$ condition. Spatial variance is evaluated using the standard method of moments [32] at each longitudinal measurement position.

Comparing both trends of the correspondent profile spatial variance in Fig. 8, results demonstrate that both measurement techniques report a similar linear trend in variance over the measurement area (slope of $a_{PCA,90} = 14.5$ and $a_{Cyclops,90} = 13.9$; this indicates that the mixing processes measured using the PCA and the Cyclops techniques are very

similar). Despite this there is a noticeable, unexpected reduction in variance recorded by the PCA above 7.5 m downstream of the injection. It is anticipated that this is caused by the direct reflection effect noted above, i.e. a lower recorded concentration value at the left side of each profile due to a region of the flume affected by a direct light reflection. This only becomes important when a significant proportion of dye spreads into the affected zone (i.e. above 7.5 m downstream of the injection). Which the apparent reduction of concentration recorded at the plume edge causing a reduction in the calculated profile variance.

Finally, ADE transverse mixing coefficients K_y were obtained from concentration measurements obtained with both PCA and Cyclops measurements. In order to obtain optimised coefficients, a simple 1D ADE transverse mixing model was used to provide concentration values over the measurement area based on measured concentration profiles at the upstream end of the measurement area, mean channel velocity values and transverse mixing coefficient (K_y). The model is based on the 1D solution to the ADE downstream of a steady vertical line source into an unbounded flow [32]. A simple optimisation routine was developed in order to identify the mixing coefficient providing the best fit between

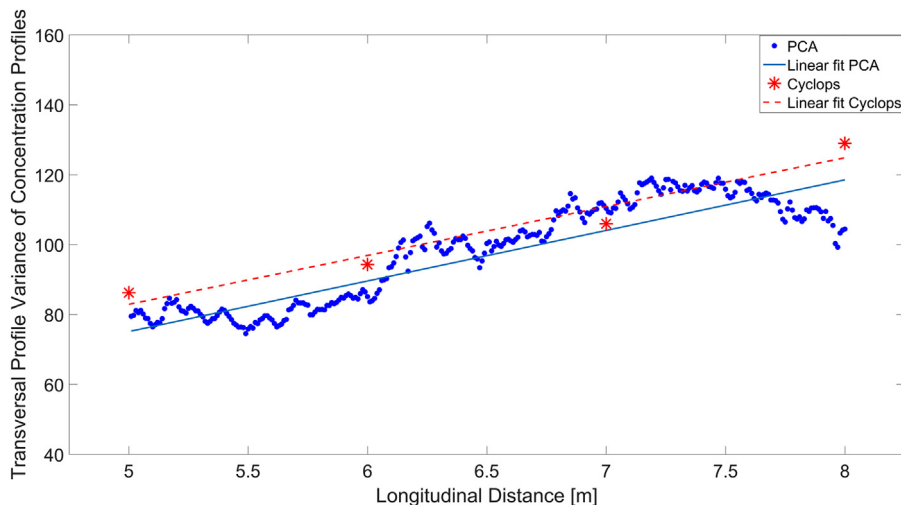


Fig. 8. Comparison between PCA and Cyclops variance (Run IV).

Table 3
Transverse mixing coefficients from PCA and Cyclops measurement techniques and coefficient of determination between data and ADE.

Test ID	K_y [m^2s^{-1}]	$\frac{K_y}{Du^*}$ [-]	R^2
Run I (PCA)	0.000118	0.271	0.958
Run II (PCA)	0.000178	0.163	0.988
Run III (PCA)	0.000248	0.138	0.970
Run IV (PCA)	0.000365	0.142	0.983
Run IV (Cyclops)	0.000381	0.143	0.994

the ADE model and the measured values over the measured area for each test and each measurement technique. The resulting (K_y), normalised ($\frac{K_y}{Du^*}$) values and the coefficient of determination (based on the MATLAB standard correlation function) between the optimised ADE model and measured values are presented in Table 3. Normalised transverse mixing coefficients were obtained using the water depth D and the calculated shear velocity $u^* = \sqrt{gDS_0}$, where S_0 = bed slope.

It can be seen that the ADE model fits the measured data well ($R^2 > 0.955$) in all cases indicating that the plume is behaving as expected when measured by both techniques. Resulting coefficients from Cyclops and PCA methods agree with a relative error of 0.7 %. Normalised values are generally within the range expected downstream for a continuous, release of solute into a wide open channel turbulent flow. This range given by [32] is $0.1 Du^*$ to $0.26 Du^*$ for straight laboratory channels. Overall the results provide confidence that the PCA technique can quantify the overall mixing processes within the channel.

2.6. Measurement accuracy (PIV)

This section considers the measurement accuracy of the system developed in this paper and aims to provide some assessment of the likely PIV measurement uncertainty. Considering the equipment used, known errors are due to a) imperfect reproduction of the spatial position of PIV particles/PCA cells due to the application of the MATLAB function as part of the spatial calibration, and b) temporal error due to the CMOS camera sensor applying a ‘rolling shutter’ effect when capturing each image frame. The spatial reproduction error varies with position, with maximum errors encountered at the edge of the images (e.g. flume sidewalls). Mean spatial errors for each camera have been previously reported in 2.3.1. When applied to the calculation of primary velocity this results in an absolute error of between 0.75% and 1.5%. Errors due to the rolling shutter effect can be estimated by considering the potential time difference within the capture of each image. In this case maximum potential errors of 0.14% in the calculation of primary velocity have been determined. The sensitivity of the velocity measurements to PIV analysis settings has also been considered. Within Dynamic Studio software both range validation (automatic removal of unfeasible velocity values) and moving average filter (to replace incorrect data points) techniques are applied. When considering a range of feasible alternate settings for a) upper and lower bound velocity (lower bound between 0.05 and 0.2 m/s, upper bound velocity between 0.6 and 0.8 m/s), b) moving average filter settings (3×3 and 5×5 data point averaging), a maximum variation in calculated primary velocity of 3.07 % was obtained (considering an example data point, 0.3 m from the sidewall, $D = 90$ mm).

Finally a primary velocity convergence analysis and reproducibility check was undertaken. Data from an example measurement point (as above) was averaged over different durations of observed data (up to 20 s). It was found that once the averaging duration exceeded 5 s of data (200 frames) the variation in calculated primary velocity values did not exceed 0.8%, and hence the measurement could be considered converged. Further testing took different 5 s periods of data from the full measurement period, and found that the maximum observed variation

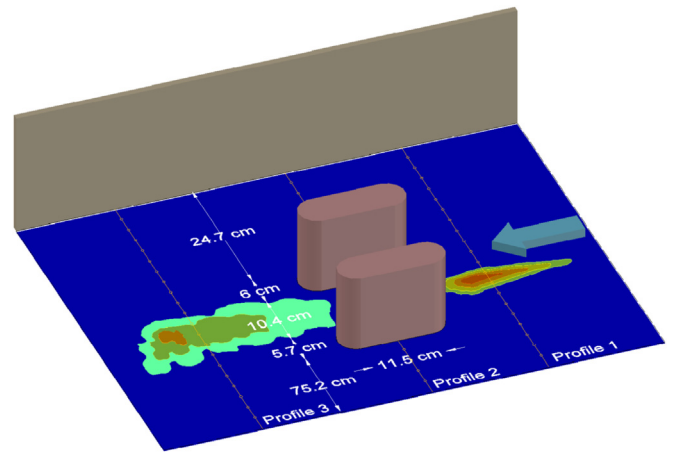


Fig. 9. Experimental configuration to verify the applicability of the GoPro Hero4 cameras for the combined PIV and PCA methods.

in the calculation of primary velocity to be 2.5%.

Considering the above errors and variations representative of the PIV measurement error, and if for a given measurement these errors are normally distributed about 0, the expected measurement error in primary velocity (taken as within one standard deviation) would be 2.15%. However it is noted that the actual measurement error of the system presented in this paper will vary between setups and flow conditions.

3. Example application

In order to demonstrate the applicability of the GoPro Hero4 cameras for the combined PIV and PCA method, an experiment was conducted in the same experimental facility described in 2.1. Two obstacles, parallel to each other, were placed as shown in Fig. 9 separated in the lateral direction by 104 mm. A pulse injection was released at the upstream section of the model using the same setup described in Section 2.2.3. Simultaneously, PIV particles were spread evenly across the upstream section of the channel by using the system described in Section 2.2.2.

All frames displayed in Fig. 10 were recorded with the water depth of 54 mm (Run II). Fig. 10 shows three different concentration frames obtained after applying the PCA technique and also the 2D velocity vectors resulting from the PIV analysis. The PIV analysis was obtained over 5 s of recorded data, taken over the same acquisition period as the PCA dataset.

The previous Sections 2.4.1 and 2.5.1 have shown that the PCA and PIV techniques perform within a reasonable tolerance; this section is designed to illustrate that both measurements can be obtained simultaneously. Nonetheless, a visual comparison between instantaneous frames and concentration maps obtained through the use of the PCA technique suggest the concentration is measured well. The total mass of each post filtering frame was observed to be within 7 %, indicating a good level of mass conservation. This is similar to levels observed in previous studies of mixing processes using traditional measurement techniques i.e. [10,39]. Furthermore, after the PIV results show a reasonable behaviour expected for a flow around an obstacle [41,20].

The primary conclusion from this section is that the PIV and PCA techniques have been successfully implemented in synchronization using a single data capture method (GoPro cameras). This confirms that the technique can be used to study the relationship between mixing processes and a local instantaneous velocity field.

4. Conclusion

This work was conducted to provide a novel cost-effective technique to simultaneously measure velocity and concentration profiles. Based

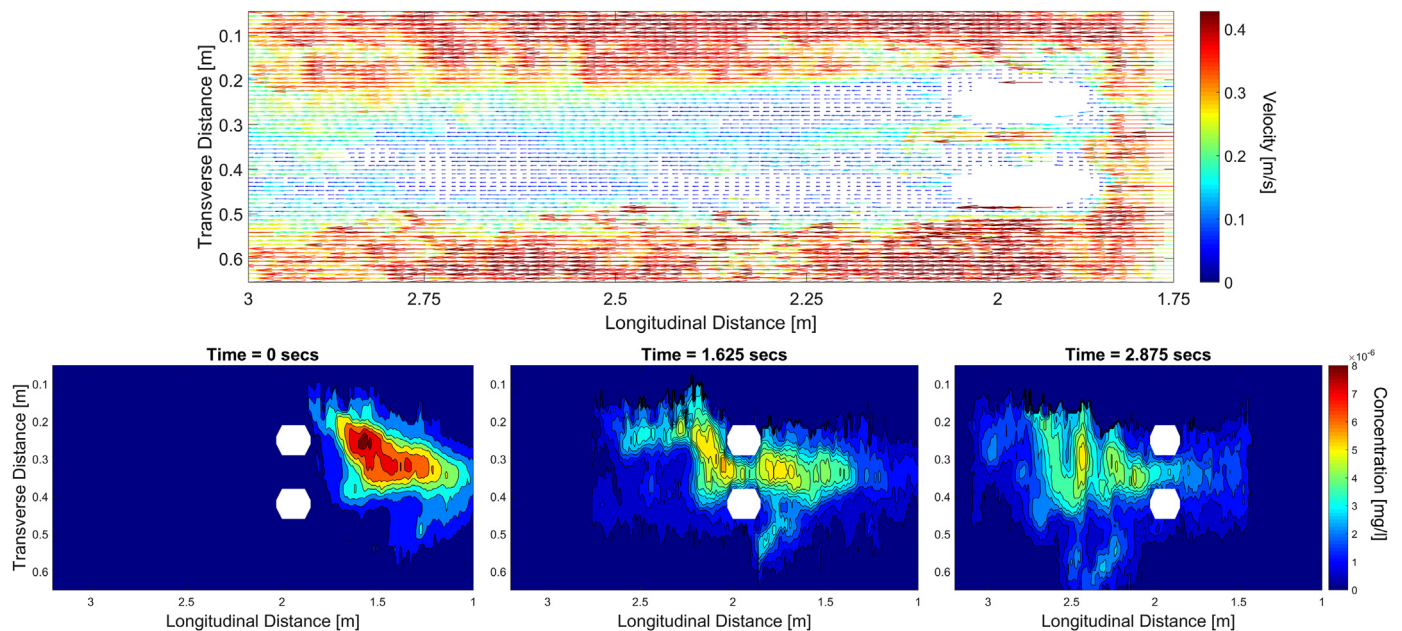


Fig. 10. Representation of instantaneous concentration maps (at 0 s, 1.625 s and 2.875 s respectively), and the corresponding mean velocity field downstream of a pulse injection.

on experiments conducted to validate the technique and explore its applications, the following conclusions are drawn:

1. GoPro Hero4 cameras were found to be suitable for measuring velocity fields and depth averaged tracer concentrations in laboratory applications over scales of 1–10 m.
2. Results obtained by applying PIV and PCA techniques to the videos recorded were validated against alternative existing measurement techniques and comparisons obtained confirmed an overall good agreement, specifically a relative error between PIV and both manual measurements and ADV of 5.17% and 4.26% respectively; and a relative difference of 0.7% between quantified transverse mixing coefficients.
3. The uncertainties associated with the estimation of the velocity field increase with the roughness of the free surface as it causes unpredictable reflections of light. For higher flow rates, turbulence is expected to be greater, generating a rougher free surface and increasing these uncertainties.
4. The influence of direct light reflections can cause error in PCA measurement in the specific areas affected. Further work is required to identify the best filtering techniques to minimise these effects. It is also recommended that the size and position of direct reflections should be considered when designing illumination/lighting setups.
5. The applicability of GoPro Hero4 cameras to combine the different measurement techniques (PCA and PIV) was successfully demonstrated by simultaneously capturing mixing and velocity profiles associated with flow between and around two emergent obstacles positioned within the flow.

The technique presented here overcomes many limitations of the existing time-consuming measurement techniques. The cameras used are inexpensive, easy to operate, non-intrusive and can be effectively used to provide continuous velocity and concentration profiles. This work has also demonstrated how possible difficulties caused by the use of multiple cameras can be resolved by externally synchronizing them and stitching together their calibrated fields of view. It is anticipated that this technique will be valuable in measuring spatially variable mixing processes in the mid field zone (prior to cross sectional mixing), or the development of a 2D concentration field downstream of a pulse

tracer release. After the success of GoPro Hero 4 cameras, many new versions with similar or better technical specifications have been launched (examples include GoPro Hero 5 and GoPro Hero 6). It is expected that following the procedure described in this paper, newer categories of camera may provide a viable and superior alternative to existing measurement techniques for laboratory and field applications.

Acknowledgements

This research was funded by Engineering and Physical Sciences Research Council (EPSRC) through the grants EP/K01952X/1 and EP/K040405/1.

References

- [1] R. Adrian, Particle-imaging techniques for experimental fluid mechanics, *Annu. Revis. Fluid Mech.* (1991) 261–304.
- [2] R. Adrian, J. Westerweel, *Particle Image Velocimetry*, Cambridge University Press, Cambridge, UK, 2011.
- [3] B. Andrews, M. Cardenas, P. Bennett, Analysis of turbulent nonisothermal mixing between a jet and cooler ambient water using thermal imagery, *Geochem. Geophys. Geosyst.* (2011).
- [4] S. Babarutsi, V.H. Chu, Dye-concentration distribution in shallow recirculating flows, *J. Hydraul. Eng.* (1991) 643–659.
- [5] R. Balachandar, V.H. Chu, J. Zhang, Experimental study of turbulent concentration flow field in the wake of a bluff body, *J. Fluids Eng.* (1997) 263–270.
- [6] R. Balachandar, M.F. Tachie, V.H. Chu, Concentration profiles in shallow turbulent wakes, *J. Fluids Eng.* (1999) 34–43.
- [7] M. Balu, R. Balachandar, H. Wood, Concentration estimation in two-dimensional bluff body wakes using image processing and neural networks, *J. Flow. Vis. Image Process.* (2001) 121–139.
- [8] Z. Botev, J. Grotowski, D. Kroese, Kernel density estimation via diffusion, *Ann. Stat.* (2010).
- [9] J. Boxall, I. Guymer, A. Marion, Transverse mixing in sinuous natural open channel flows, *J. Hydraul. Res.* (2003).
- [10] J.B. Boxall, I. Guymer, Estimating transverse mixing coefficients, *Proc. Inst. Civil Eng. - Water Marit. Eng.* (2000).
- [11] S.M. Cameron, V.I. Nikora, I. Albayrak, O. Miler, M. Stewart, F. Siniscalchi, Interactions between aquatic plants and turbulent flow: a field study using stereoscopic piv, *J. Fluid Mech.* (2013) 345–372, <https://doi.org/10.1017/jfm.2013.406>.
- [12] M. Cardenas, C. Neale, C. Jaworowski, H. Heasler, High-resolution mapping of river-hydrothermal water mixing: Yellowstone National Park, *Int. J. Remote Sens.* (2009).
- [13] C. Carmer, A. Rummel, G. Jirka, Mass transport in shallow turbulent wake flow by planar concentration analysis technique, *J. Hydraul. Eng.* (2009) 257–270.
- [14] V.H. Chu, J.B. Zhang, Starting jets in a double-tank apparatus shallow flows, *Selected Papers of the International Symposium on Shallow Flows*, Balkema,

- Leiden, The Netherlands, 2004, pp. 71–78.
- [15] J.F. Clark, P. Schlosser, M. Stute, H.J. Simpson, SF6-3He tracer release experiment: a new method of determining longitudinal dispersion coefficients in large rivers, *Environ. Sci. Technol.* (1996) 1527–1532.
- [16] J. Hove, R. Koster, A. Forouhar, G. Acevedo-Boltion, S. Fraser, M. Gharib, Intracardiac fluid forces are an essential epigenetic factor for embryonic cardio genesis, *Nature* (2003) 172–177.
- [17] M. Islam, D. Zhu, A kernel density based algorithm to despiked adv data, *J. Hydraul. Eng.* (2013).
- [18] J. Katz, J. Sheng, Applications of holography in fluid mechanics and particle dynamics, *Annu. Revis. Fluid Mech.* (2010).
- [19] R.D. Keane, R. Adrian, Particle-imaging velocimetry, *Meas. Sci. Technol.* (1991).
- [20] C. Li, M. Zhang, Numerical modeling of shallow water flow around arrays of emergent cylinders, *J. Hydro-Environ. Res.* (2010).
- [21] MATLAB and Statistics Toolbox Release, The MathWorks, Inc., Natick, 201 Massachusetts, United States (2017a).
- [22] M. McNutt, R. Camilli, T. Crone, G. Guthrie, P. Hsieh, Review of flow rate estimates of the deepwater horizon oil spill, *Proc. Natl. Acad. Sci. U.S.A.* (2012).
- [23] M. McNutt, R. Camilli, G. Guthrie, V. Labson, B. Lehr, Assessment of flow rate estimates for the deepwater horizon/macondo well oil spill flow rate, National Incident Command, 2011.
- [24] L. Melton, C. Lipp, Criteria for quantitative PLIF experiments using high-power lasers, *Exp. Fluids* (2003).
- [25] M. Murphy, R. Adrian, Piv through moving shocks with refracting curvature, *Exp. Fluids* (2011) 847–862.
- [26] M. Muste, A. Hauet, I. Fujita, C. Legout, H. Ho, Capabilities of Large-scale Particle Image Velocimetry to characterize shallow free-surface flows, *Adv. Water Resour.* (2014).
- [27] G. Novak, G. Rak, T. Preseren, T. Bajcar, Non-intrusive measurements of shallow water discharge, *Flow. Meas. Instrum.* (2017).
- [28] A. Pilechi, A. Mohammadian, C.D. Rennie, D.A. Zhu, Efficient method for coupling field data and numerical modeling for the estimation of transverse mixing coefficients in meandering rivers, *J. Hydraul. Eng.* (2016).
- [29] M. Raffel, C. Willert, J. Kompenhans, *Particle Image Velocimetry: A Practical Guide*, Springer, Berlin, 1998.
- [30] D. Rosgen, A classification of natural rivers, *Catena* (1994) 169–199.
- [31] A. Rummel, C. Carmer, H. Gerhard, Combined planar measurements of flow velocity and mass concentration in shallow turbulent flow part 1: development of a planar concentration analysis (PCA) system, in: *Proceedings of Hydraulic Measurement and Experimental Methods Specialty Conference (HMEM)* (2002).
- [32] J. Rutherford, *River Mixing*, J. Wiley and Sons Ltd, New York, 1994.
- [33] J. Santiago, S. Wereley, D. Meinhart, C.D. and Beebe, R. Adrian, A particle image velocimetry system for microfluidics, *Experiments in fluids* (1998) pp. 316–319.
- [34] I. Seo, M. Lee, K. Baek, 2D Modeling of heterogeneous dispersion in meandering channels, *J. Hydraul. Eng.* (1994).
- [35] I.W. Seo, K.O. Beak, T.M. Jeon, Analysis of transverse mixing in natural streams under slug tests, *J. Hydraul. Res.* (2006) 350–362.
- [36] I.W. Seo, H.J. Choi, Y.D. Kim, E.J. Han, Analysis of two dimensional mixing in natural streams based on transient tracer tests, *J. Hydraul. Eng.* (2016).
- [37] T. Serra, H. Fernando, R. Rodriguez, Effects of emergent vegetation on lateral diffusion in wetlands, *Water Res.* (2004).
- [38] J. Shucksmith, J. Boxall, I. Guymer, Effects of emergent and submerged natural vegetation on longitudinal mixing in open channel flow, *Water Resour. Res.* (2010).
- [39] J. Shucksmith, J.B. Boxall, I. Guymer, Importance of advective zone in longitudinal mixing experiment, *Acta Geophys.* (2007).
- [40] P. Smart, I. Laidlaw, An evaluation of some fluorescent dyes for water tracing, *Water Resour. Res.* (1977).
- [41] C. Song, M. Yuan, Simulation of vortex-shedding flow about a circular cylinder at high Reynolds numbers, *J. Fluids Eng.* (1990).
- [42] F. Sonnenwald, J. Hart, P. West, V. Stovin, I. Guymer, Transverse and longitudinal mixing in real emergent vegetation at low velocities, *Water Resour. Res.* (2017).
- [43] S. Stone, C. Meinhart, S. Wereley, A microfluidic-based nanoscope, *Exp. Fluids* (2002) 613–619.
- [44] P. Tokumaru, P. Dimotakis, Image correlation velocimetry, *Exp. Fluids* (1995) 1–15.
- [45] C. Tropea, A. Yarin, J. Foss, *Handbook of Experimental Fluid Mechanics*, Springer, New York, 2007.
- [46] P. Vennemann, K. Kiger, R. Lindken, B. Groenendijk, S. Stekelenburg-de Vos, In vivo microparticle image velocimetry measurements of blood-plasma in the embryonic avian heart, *J. Biomech.* (2006) 1191–1200.
- [47] P. Ward, Measurement of dye concentration by photography, *J. Environ. Eng. Div.* (1973) 165–175.
- [48] V. Weitbrecht, G. Kühn, G.H. Jirka, Large scale piv-measurements at the surface of shallow water flows, *J. Flow. Meas. Instrum.* (2002) 237–245.
- [49] S. Wereley, C. Meinhart, Recent advances in micro-particle image velocimetry, *Annu. Revis. Fluid Mech.* (2010).
- [50] C. Willert, M. Gharib, Digital particle image velocimetry, *Exp. Fluids* (1991) 181–193.
- [51] J.B. Zhang, V.H. Chu, Shallow turbulent flows by video imaging method, *J. Eng. Mech.* (2003) 1164–1172.
- [52] Y. Zeng, W. Huai, I. Guymer, Transverse Mixing in a Trapezoidal Compound Open Channel, *J. Hydrodyn.* (2008).